ELSEVIER

Nuclear Physics A 705 (2002) 3–28

NUCLEAR PHYSICS A

www.elsevier.com/locate/npe

High-spin states in the odd–odd nucleus ^{80}Y

D. Bucurescu [a,*], C.A. Ur [a,b], M. Ionescu-Bujor [a], A. Iordăchescu [a], D. Bazzacco [b], F. Brandolini [b], G. de Angelis [c], M. De Poli [c], A. Gadea [c], S. Lunardi [b], N. Mărginean [a,c], N.H. Medina [b,1], D.R. Napoli [c], P. Pavan [b], C. Rossi Alvarez [b], P. Spolaore [c]

[a] *National Institute for Physics and Nuclear Engineering, Bucharest, Romania*
[b] *Dipartimento di Fisica dell'Universita and INFN, Padova, Italy*
[c] *INFN, Laboratori Nazionali di Legnaro, Legnaro, Italy*

Received 20 December 2001; accepted 11 January 2002

Abstract

The high-spin states of ^{80}Y have been studied with the reactions ^{24}Mg(^{58}Ni, pnγ) at 180 MeV and ^{58}Ni(^{24}Mg, pnγ) at 77 MeV. Gamma-ray transitions in this nucleus have been unambiguously assigned by using the GASP detector array in conjunction with the recoil mass spectrometer CAMEL and the ISIS Silicon detector ball. These transitions have been arranged into several rotational bands extending up to an excitation energy of about 12 MeV and spin 24 $\hbar$. The bands are discussed within the framework of the interacting boson–fermion–fermion and cranked shell models.

PACS: 21.10.Re; 21.60.Ev; 23.20.Lv; 27.50.+e

Keywords: NUCLEAR REACTIONS ^{24}Mg(^{58}Ni, pnγ), $E = 180$ MeV; ^{58}Ni(^{24}Mg, pnγ), $E = 77$ MeV; Measured E_γ, $I_\gamma(\theta)$, DCO ratios, γ–γ, charged-particle–γ and recoil–γ coincidences; ^{80}Y deduced levels, J^π, rotational bands, B(M1)/B(E2) ratios; Interacting boson–fermion–fermion-model calculations; Cranked shell model description

* Corresponding author.
E-mail address: bucurescu@tandem.nipne.ro (D. Bucurescu).

[1] Supported by CNPq, Brasil.

0375-9474/02/$ – see front matter
PII: S0375-9474(02)00623-1

1. Introduction

The neutron deficient nuclei from the region with N and $Z \approx 38$ to 40 have been a subject of continuous interest during the last years. In this region, the shell model orbitals develop gaps at large deformation for the nucleon numbers 38 and 40 [1] and, since the neutrons and protons occupy the same orbitals the effects of these gaps are quite strong. Thus, an 'island' of nuclei with large prolate deformation in the ground state ($\beta_2 \approx 0.4$) has been discovered at $N, Z = 38$ and 40 [2,3]. Also, since the density of shell model orbitals in these nuclei is not high, dramatic shape changes take place with small changes in the nucleon numbers. The same happens with increasing spin, where phenomena such as particle alignments and blocking effects are associated with different shape transitions. Another point of interest in this region close to the $N = Z$ line is the study of the effects of the neutron–proton pairing, and especially the competition between its $T = 0$ and $T = 1$ components.

The nuclei in this remote region are usually populated with rather small cross sections in the heavy-ion induced reactions available with stable targets and projectiles. In the case of the odd–odd nuclei, this difficulty adds to the fact that they have rather complicated level schemes. In studying such nuclei it is, therefore, imperiously necessary to use very efficient procedures for identifying the weak channels of interest, and this is possible only with a large Ge detector array in conjunction with ancillary detectors.

In this work, we present in-beam gamma-ray spectroscopy results for the odd–odd ^{80}Y nucleus which lies in the immediate vicinity of the most deformed $A \approx 80$ nuclei. Preliminary results concerning several rotational bands identified in this nucleus have been published in Ref. [4]. With new measurements, we have completed and extended the high-spin level scheme. Recent complementary studies [5–8] brought important clarifications concerning the low-energy part of the level scheme. The observed structures in ^{80}Y are discussed on the basis of the interacting boson–fermion–fermion model (IBFFM) and of the cranked shell model (CSM).

2. Experimental details and results

2.1. The measurements

High-spin states in the odd–odd ^{80}Y nucleus were populated first in the 'inverse kinematics' reaction ^{24}Mg(^{58}Ni, pnγ) at an incident energy of 180 MeV. In this case the target was a self supporting ^{24}Mg foil of 0.5 mg/cm^2. Preliminary results of this experiment have been published in Ref. [4]. A second, complementary experiment has then been performed with the ^{58}Ni(^{24}Mg, pnγ) reaction at the incident energy of 77 MeV, using as target a stack of two 0.5 mg/cm^2 ^{58}Ni foils. In this reaction the recoil nuclei had lower velocities, leading to gamma-ray spectra less affected by Doppler broadening, which allowed the extension of the level scheme in the region of high-energy gamma rays. The results reported in this paper are mainly based on this second experiment.

The experiments were performed at the XTU Tandem accelerator of the National Laboratories of Legnaro. The beam currents were about 12 and 5 pnA in the ^{58}Ni and

^{24}Mg beam experiments, respectively. The beam energy was chosen such as to optimize the population of the channels with two evaporated particles. This resulted in a relatively small number of opened reaction channels and consequently a lower degree of complexity of the gamma-ray spectra.

The gamma rays were detected with the GASP array [9] consisting of 40 large volume Compton suppressed HPGe detectors and an 80 BGO element inner ball acting as a gamma-ray calorimeter. Gain matching and energy and efficiency calibration of the Ge detectors were performed by using standard radioactive sources of ^{56}Co, ^{133}Ba, and ^{152}Eu. The light charged particles evaporated from the compound nucleus were detected and identified with the 4π ISIS detector [10], consisting of 40 ΔE–E Si telescopes and placed in the center of the GASP array. In the Ni-beam experiment, the recoils exiting from the target were separated with the recoil mass spectrometer CAMEL (RMS) [11] and detected with its focal plane detector. At the time of the experiment the focal plane detector consisted of a multiwire Parallel Plate Avalanche Counter (PPAC) having active sizes of 12 cm horizontally and 8 cm vertically, with a distance of 1 mm between the wires. For the ISIS detector we estimated an efficiency of 50% for the detection of one proton. In the case of the RMS, the efficiency for the detection of mass 80 recoils was estimated to be about 1%.

Data were collected on tape only when at least two Ge detectors and two BGO elements fired in coincidence. The information from ISIS and CAMEL systems was recorded whenever the trigger condition was fulfilled. With this way of storage, in the off-line analysis we could include or disregard the information coming from these detector systems. A total of 1.34×10^9 double- and 2×10^8 triple-coincidence events were collected in the second ('direct kinematics' reaction) measurement.

2.2. Mass separation and identification of the ^{80}Y channel

The RMS was set so that only one charge state was recorded in the centre of the PPAC detector for the masses 79 and 80 while for the other masses two charge states were detected. Fig. 1 shows a two-dimensional plot of the mass separation (the x-coordinate of

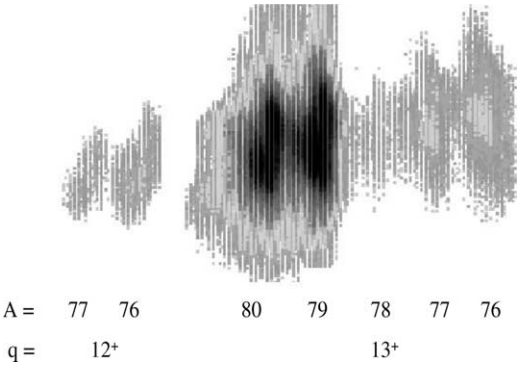

Fig. 1. Mass spectrum observed with the PPAC in the focal plane of the RMS. The horizontal coordinate is the position in the focal plane—corresponding to an opening of 12 cm, and the vertical one is the time of flight of the recoils.

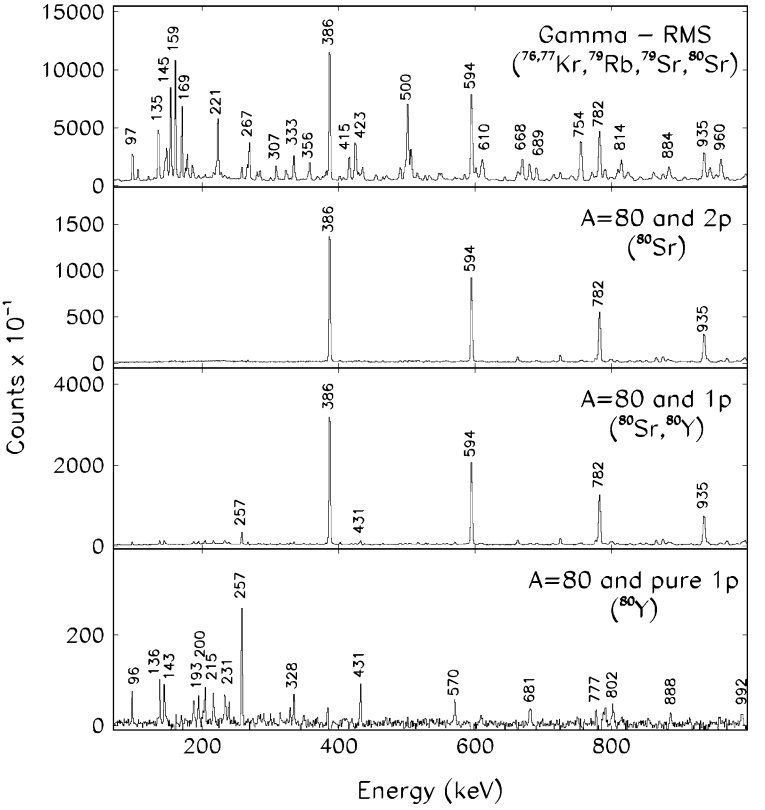

Fig. 2. Spectra demonstrating the identification of the gamma-ray transitions in ^{80}Y. First (upper) panel: gamma-ray spectrum coincident with all recoils detected in the focal plane of the RMS; second: spectrum coincident with mass 80 *and* two protons detected in ISIS; third: spectrum coincident with mass 80 *and* one proton in ISIS; fourth (last panel): spectrum coincident with mass 80 and one proton, but cleaned of the contribution of the 2p channel.

the PPAC detector) against the time of flight. The events from the RMS are predominantly coming from the two central peaks corresponding to charge 13^+ of mass 80 (left side) and mass 79 (right side). The smaller islands on the sides of these two large peaks correspond to the masses 76 and 77.

In the conditions of our experiments, gamma rays could be unambiguously assigned to the various produced nuclei on the basis of the coincidences with the mass identified in the PPAC detector, with various combinations of the charged particles identified by ISIS, as well as with known gamma rays.

Fig. 2 illustrates the way in which prompt gamma rays have been assigned to the ^{80}Y nucleus (the pn channel). The upper panel shows the gamma-ray spectrum coincident with all recoil events detected by the RMS. This spectrum is dominated by transitions in the indicated nuclei, populated mainly in two- and three-particle evaporation channels. The next panel gives the gamma-ray spectrum coincident with mass 80 *and* two protons detected by ISIS; it contains only transitions of the ^{80}Sr nucleus (the 2p channel). In the

next panel is a spectrum coincident with mass 80 *and* one proton; this spectrum contains again transitions of ^{80}Sr, and, presumably, of ^{80}Y (readily visible such candidate transitions are those at 257 and 431 keV). By using the determined proton detection efficiency, the two spectra could be normalized and subtracted such as to remove the contribution of ^{80}Sr; the result is given in the spectrum from the lowest panel of Fig. 2, which thus contains gamma rays unambiguously assigned to transitions in ^{80}Y. Among these gamma rays is also the 257 keV one, assigned before to ^{80}Y [3].

2.3. The construction of the level scheme

The 257 keV gamma ray is the strongest transition assigned to ^{80}Y (see Fig. 2), and, therefore, it was assumed to feed the ground state of this nucleus. The level scheme has then been constructed in the usual way, based on γ–γ coincidence relationships observed either in the proton-gated γ–γ matrix or in a γ–γ–γ cube, and relative gamma-ray intensities.

The deduced level scheme is given in Fig. 3. We emphasize that this figure shows the whole up-to-date information, as it contains also the results of several other experiments [5–8] which followed our measurement reported in [4] and cleared up the situation of the low-lying isomeric states. As a result of the present measurements, all bands have been followed to much higher spins than reported in our previous communication [4]. Both signatures of band 1 are reported now. The beginning of another band structure (band 2) feeding into the 13^- level of band 1 has also been observed. In our previous publication [4], band 4 has been placed in position (excitation energy) only by means of the 315 keV transition which connects it to band 3. The band position is now more firmly established by the observation of other two transitions, of 114 and 474 keV, connecting it to different states of band 3. In this way, the position of band 5, which is connected by many transitions to band 4, is also more firmly established. In our experiments, as stated in the previous work and as obvious from the above remarks, it is found that band 5 stops on a level with excitation energy 312 keV, assumed to be an isomeric level. Also, band 6, firmly assigned to ^{80}Y, was left as a 'floating' band assumed to be built on another isomeric state [4]. Subsequent researches have indeed identified two isomeric levels. The works of Regan et al. [5] and Chandler et al. [7] reported an isomer with half-life of 4.2 μs which decays by an 84 keV transition. Döring et al. [6] found another isomer, with a half-life of 4.7 s, assigned to an excited state at 228 keV which decays to the ground state, and proposed that the 84 keV transition links the two isomeric states. Thus, they identified the 4.2 μs isomer with the head of our band 5, while the 228 keV level was proposed as the head of our band 6 (numbered as bands 7 and 8, respectively, in our previous paper [4]). In this way, the excitation energy given by us for the head of band 5 was independently confirmed, and a plausible way of solving the puzzle of the 'floating' bands observed in the in-beam experiments was proposed. Another very recent experiment, using an isomer decay tagging technique, showed that our band 5 is indeed built on the isomer which decays by the 84 keV transition [8]. Coincidence spectra obtained with appropriate gamma-ray gates are shown in Figs. 4 and 5 to illustrate both the negative and positive-parity bands observed in our experiments.

Before commenting on the gamma-ray multipolarities and the spin–parity assignments, we first give the present status of knowledge concerning the spin and parity of some

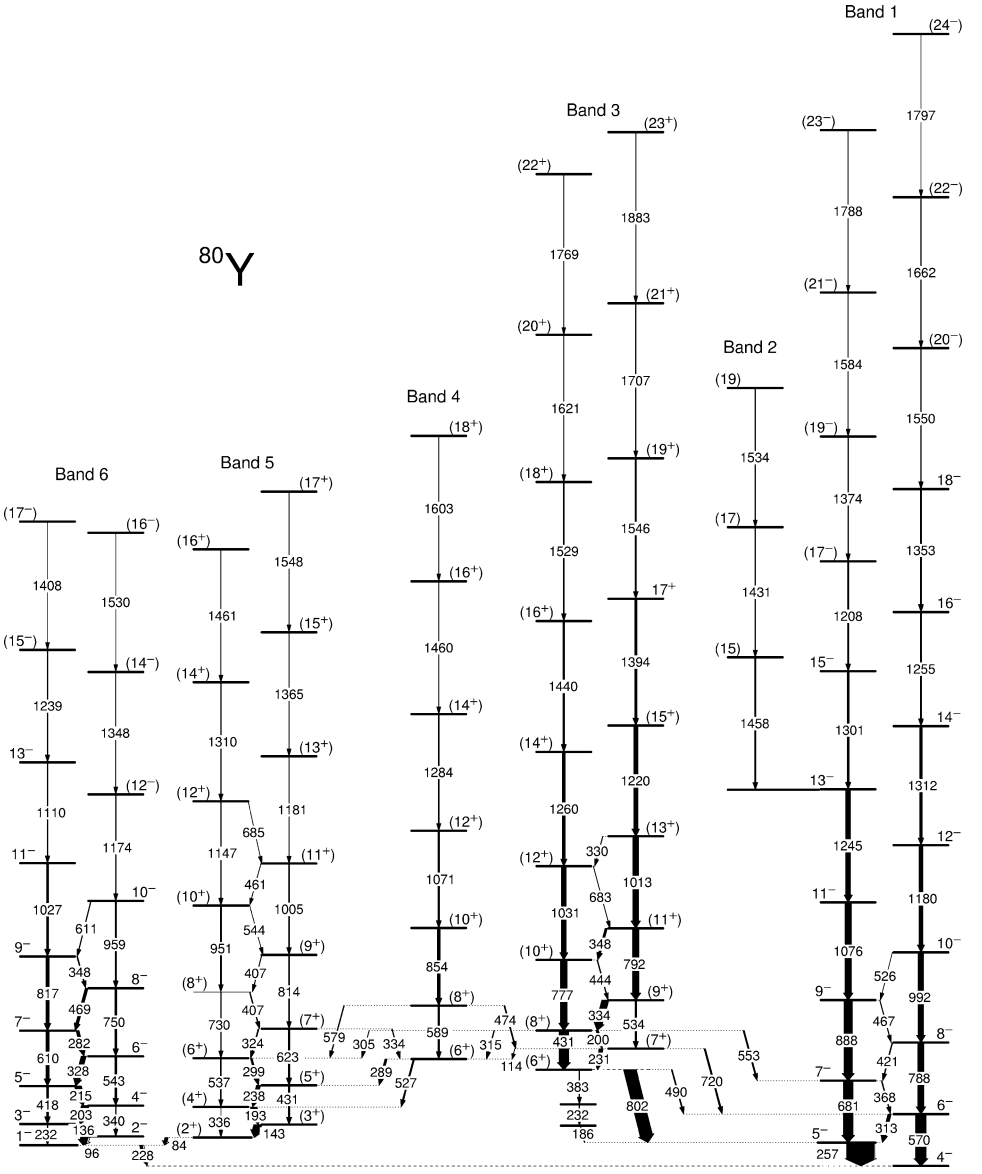

Fig. 3. Level scheme of ^{80}Y as determined from the present experiments. The position of the isomeric level at 228 keV and its transition towards the ground state, the transition of 84 keV, and the spin–parity assignments for the two isomeric levels at 228 and 312 keV are those adopted in Refs. [5,6,8,14,15].

of the low-lying states of ^{80}Y. Previous β-decay work suggested that the ground state of ^{80}Y has $J^\pi = 4^-$ [12,13]. A recent detailed β-decay study [14] used the observed β-decay fragmentation and the log *ft* values to assign $J^\pi = 4^-$ to the ground state, and 1^- to the 228 keV isomeric level, thus supporting the M3 character of the 228 keV

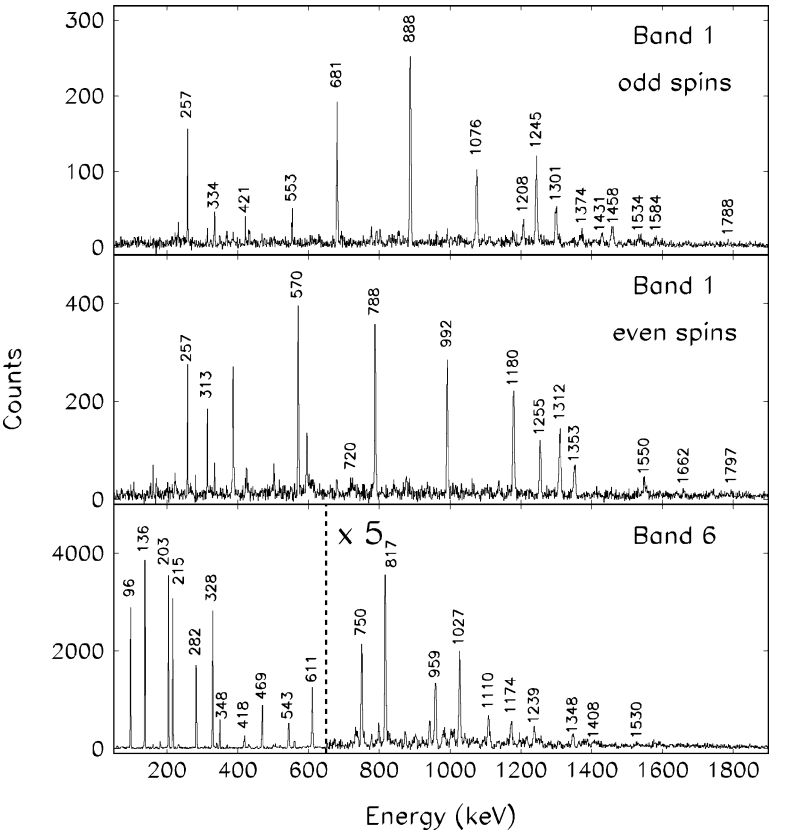

Fig. 4. Gamma-ray spectra illustrating the negative-parity bands 1 and 6 from Fig. 3. These are spectra obtained by sums of double gates in the γ–γ–γ cube, set on transitions assigned to the bands.

transition proposed in Ref. [6]. The multipolarity of the 228 keV transition has also been directly determined as M3, from internal conversion coefficient measurements [15,16]. Consequently, there are firm J^{π} assignments for the ground state and the 228 keV isomeric state. For the isomeric state at 312 keV, Döring et al. [6] suggested (2^{+}), which did not agree with our previous tentative assignment of (3^{-}) [4] based on some DCO ratios with large errors and a certain similarity of band 5 with the negative-parity bands known in ^{82}Y [17–19]. Our new data support the assignment of Ref. [6] (see discussion below).

Information concerning the gamma-ray multipolarities has been obtained in our experiments from gamma-ray angular distributions (determined from the seven rings of detectors between 36° and 144° [9]) and DCO ratios (deduced from the detector rings at 36°, 144° and 90°). The gamma-ray intensities, DCO ratios, angular distribution coefficients A_2/A_0 and A_4/A_0, as well as the transition assignments, are given in Table 1. For most of the lowest transitions the multipolarity is quite obvious. Thus, in band 1, the 257 and 313 keV transitions have a dipole character, while 570, 681, 788 keV, etc., are quadrupoles. We assumed that these are M1 and E2 transitions, respectively, and

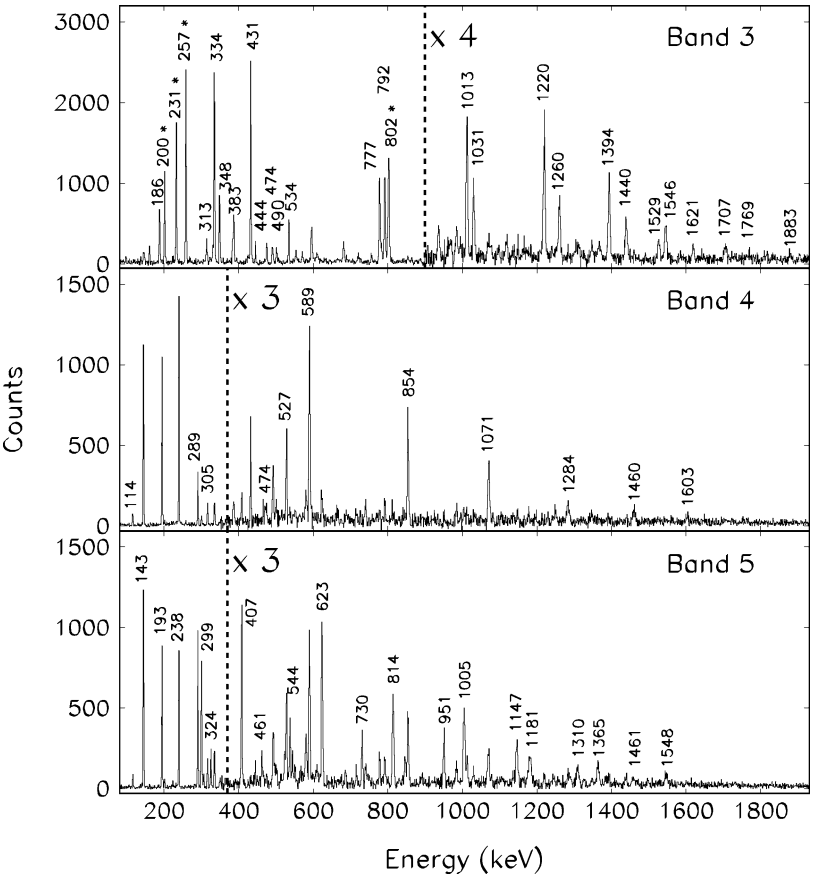

Fig. 5. Same as Fig. 4, but for the positive-parity bands 3, 4 and 5 from Fig. 3.

correspondingly we assigned negative parity to the states in band 1. The dipole character of the transition of 802 keV establishes a spin (6) for the head of band 3. The transitions between the two signatures (231, 200, 334, 348 keV) have clear dipole character, while the in-band ones (431, 534, 777, 792 keV) are quadrupoles. Positive parity has been assigned to this band on the basis of its similarity with the positive-parity bands well known in ^{82}Y and ^{84}Y [17–21]. Band 5 is based, as stated above, on a (2^+) isomeric state and the interweaving of dipole and quadrupole transitions (Table 1) within this structure leads to the assignment of the two signature partner bands of positive parity. For band 4, one can start now from states in both band 5 and band 3 with which its lowest two states are connected (Fig. 2). The multipolarities of these connecting transitions support the spin assignments of (6) and (8), respectively, for these two states (Table 1). For this quadrupole band one could not identify a signature partner. Its positive parity is assumed on the basis of its multiple connections only with the positive-parity bands 3 and 5. Finally, the multipolarities of the transitions in band 6, based on the 1^- state, attest the negative parity of the two bands which belong to this structure.

Table 1
Gamma-ray intensities, DCO ratios and/or angular distribution coefficients, and spin–parity assignments for excited states in ^{80}Y. The data correspond to the reaction ^{58}Ni(^{24}Mg, pnγ) at 77 MeV

	E_γ	Intensity[a]	R_{DCO}[b]	$A_2/A_\circ$	$A_4/A_\circ$	Assignment[c]
Band 1	257.0	100.0(33)	$1.0(1)_{(D)}$	−0.12(3)	+0.06(5)	$5^- \to 4^-$
	312.9	11.8(14)	$0.6(1)_{(Q)}$	−0.17(5)	+0.13(10)	$6^- \to 5^-$
	367.6	3.1(12)				$7^- \to 6^-$
	421.2	3.0(4)				$8^- \to 7^-$
	466.6	1.9(6)				$9^- \to 8^-$
	525.9	0.5(1)	$1.6(6)_{(D)}$			$10^- \to 9^-$
	570.1	38.9(44)		+0.12(5)	+0.06(8)	$6^- \to 4^-$
	680.6	35.0(8)		+0.19(3)	−0.05(5)	$7^- \to 5^-$
	788.4	22.7(11)	$1.8(1)_{(D)}$	+0.24(5)	−0.03(7)	$8^- \to 6^-$
	887.6	31.8(8)		+0.24(3)	−0.17(5)	$9^- \to 7^-$
	992.3	19.9(14)	$0.9(2)_{(Q)}$	+0.26(6)	−0.24(9)	$10^- \to 8^-$
	1076.0	23.1(73)		+0.49(4)	+0.20(7)	$11^- \to 9^-$
	1180.1	14.0(12)		+0.35(8)	−0.14(12)	$12^- \to 10^-$
	1208.2	4.4(7)				$(17^-) \to 15^-$
	1244.9	17.5(13)		+0.31(5)	+0.08(8)	$13^- \to 11^-$
	1255.0	5.3(10)		+0.48(29)	−0.17(36)	$16^- \to 14^-$
	1300.6	7.2(5)		+0.45(9)	+0.09(12)	$15^- \to 13^-$
	1311.5	8.4(10)		+0.20(8)	+0.06(13)	$14^- \to 12^-$
	1352.6	5.4(7)		+0.27(14)	−0.20(22)	$18^- \to 16^-$
	1374.3	2.6(4)				$(19^-) \to (17^-)$
	1550.4	3.2(6)				$(20^-) \to 18^-$
	1583.5	1.3(3)				$(21^-) \to (19^-)$
	1662.5	1.3(5)				$(22^-) \to (20^-)$
	1788	0.6(4)				$(23^-) \to (21^-)$
	1797.0	0.6(4)				$(24^-) \to (22^-)$
Band 2	1430.6	2.4(4)				$(17) \to (15)$
	1457.5	4.8(7)		+0.37(15)	+0.19(23)	$(15) \to (13)$
	1534.5	1.8(4)				$(19) \to (17)$
Band 3	200.0	8.7(9)		−0.59(4)	+0.06(8)	$(8^+) \to (7^+)$
	231.0	14.6(6)	$1.2(2)_{(D)}$	−0.36(5)	+0.04(9)	$(7^+) \to (6^+)$
	329.5	1.7(4)				$(13^+) \to (12^+)$
	333.5	24.8(16)	$0.6(1)_{(Q)}$	−0.51(5)	+0.07(10)	$(9^+) \to (8^+)$
	347.6	8.0(7)	$0.6(1)_{(Q)}$	−0.46(6)	+0.15(10)	$(11^+) \to (10^+)$
	431.3	35.9(6)	$0.8(3)_{(D)}$	+0.12(3)	−0.04(4)	$(8^+) \to (6^+)$
	443.9	2.7(4)				$(10^+) \to (9^+)$
	533.7	6.3(6)		+0.34(11)	−0.14(11)	$(9^+) \to (7^+)$
	683.4	1.0(3)				$(12^+) \to (11^+)$
	777.3	25.4(6)		+0.29(3)	−0.10(51)	$(10^+) \to (8^+)$
	791.5	24.8(60)		+0.25(6)	+0.01(10)	$(11^+) \to (9^+)$
	1012.8	22.0(52)		+0.46(6)	+0.11(8)	$(13^+) \to (11^+)$
	1030.6	16.8(39)	$0.8(2)_{(Q)}$	+0.39(7)	+0.04(9)	$(12^+) \to (10^+)$
	1220.3	15.1(9)		+0.30(6)	+0.10(9)	$(15^+) \to (13^+)$
	1260.3	9.9(10)		+0.36(13)	−0.06(19)	$(14^+) \to (12^+)$
	1394.3	7.9(5)				$(17^+) \to (15^+)$
	1440.1	5.6(8)		+0.45(8)	+0.18(11)	$(16^+) \to (14^+)$
	1529.0	2.8(6)				$(18^+) \to (16^+)$
	1546.3	4.5(5)				$(19^+) \to (17^+)$
	1620.8	1.3(4)				$(20^+) \to (18^+)$

Table 1 (*continued*)

	E_γ	Intensity[a]	R_{DCO}[b]	$A_2/A_\circ$	$A_4/A_\circ$	Assignment[c]
	1707.0	1.7(4)				$(21^+) \rightarrow (19^+)$
	1768.9	0.5(3)				$(22^+) \rightarrow (20^+)$
	1882.6	0.8(4)				$(23^+) \rightarrow (21^+)$
Band 4	588.9	5.2(2)		+0.26(6)	−0.09(9)	$(8^+) \rightarrow (6^+)$
	853.9	9.8(39)		+0.29(6)	−0.24(9)	$(10^+) \rightarrow (8^+)$
	1071.2	4.9(4)		+0.28(17)	−0.26(26)	$(12^+) \rightarrow (10^+)$
	1284.0	1.6(3)		+0.57(22)	+0.09(34)	$(14^+) \rightarrow (12^+)$
	1459.6	1.7(4)				$(16^+) \rightarrow (14^+)$
	1602.8	0.8(3)				$(18^+) \rightarrow (16^+)$
Band 5	143.0	20.0(25)	$0.8(2)_{(Q)}$	−0.14(2)	−0.07(3)	$(3^+) \rightarrow (2^+)$
	192.9	23.1(12)	$1.1(1)_{(D)}$	−0.09(3)	−0.02(3)	$(4^+) \rightarrow (3^+)$
	237.9	14.7(30)	$1.0(1)_{(D)}$	−0.14(3)	0.00(5)	$(5^+) \rightarrow (4^+)$
	299.2	6.5(1)	$0.9(4)_{(Q)}$	−0.05(4)	+0.02(8)	$(6^+) \rightarrow (5^+)$
	323.9	3.5(1)	$1.0(3)_{(D)}$	−0.26(11)	+0.10(21)	$(7^+) \rightarrow (6^+)$
	336.1	0.7(1)		+0.18(12)	+0.10(16)	$(4^+) \rightarrow (2^+)$
	406.6	3.1(1)				$(8^+) \rightarrow (7^+)$
	406.8	1.6(5)				$(9^+) \rightarrow (8^+)$
	431.1	6.0(2)	$0.9(2)_{(Q)}$			$(5^+) \rightarrow (3^+)$
	461.2	0.9(2)				$(11^+) \rightarrow (10^+)$
	537.0	3.3(1)	$1.2(3)_{(D)}$	+0.20(10)	−0.02(17)	$(6^+) \rightarrow (4^+)$
	543.7	0.6(2)		+0.26(6)	−0.02(8)	$(10^+) \rightarrow (9^+)$
	623.0	6.3(13)	$1.7(9)_{(D)}$	+0.23(13)	−0.01(16)	$(7^+) \rightarrow (5^+)$
	685.3	0.6(3)				$(12^+) \rightarrow (11^+)$
	730.5	2.9(1)	$0.8(3)_{(D)}$	+0.14(19)	−0.24(30)	$(8^+) \rightarrow (6^+)$
	813.8	4.1(16)		+0.21(32)	−0.31(51)	$(9^+) \rightarrow (7^+)$
	951.0	3.8(12)				$(10^+) \rightarrow (8^+)$
	1005.0	3.9(3)		+0.27(10)	+0.01(15)	$(11^+) \rightarrow (9^+)$
	1147.0	2.9(5)				$(12^+) \rightarrow (10^+)$
	1180.1	14.0(12)		+0.35(8)	−0.14(12)	$(13^+) \rightarrow (11^+)$
	1309.6	2.6(4)				$(14^+) \rightarrow (12^+)$
	1365.3	1.5(3)				$(15^+) \rightarrow (13^+)$
	1461.4	1.3(3)				$(16^+) \rightarrow (14^+)$
	1547.7	0.9(2)				$(17^+) \rightarrow (15^+)$
Band 6	95.5	27.0(30)		−0.12(3)	−0.07(6)	$2^- \rightarrow 1^-$
	136.2	31.9(28)		−0.16(4)	−0.06(6)	$3^- \rightarrow 2^-$
	203.0	27.2(14)		−0.17(5)	−0.05(8)	$4^- \rightarrow 3^-$
	215.1	24.1(15)		−0.18(5)	+0.02(9)	$5^- \rightarrow 4^-$
	232.4	2.1(8)				$3^- \rightarrow 1^-$
	281.6	10.9(10)		−0.23(3)	+0.07(5)	$7^- \rightarrow 6^-$
	328.2	17.7(15)		−0.22(3)	−0.01(45)	$6^- \rightarrow 5^-$
	339.7	2.7(3)		+0.19(9)	−0.04(13)	$4^- \rightarrow 2^-$
	348.4	3.3(4)		−0.24(6)	−0.09(9)	$9^- \rightarrow 8^-$
	418.0	7.2(4)		+0.28(14)	+0.07(21)	$5^- \rightarrow 3^-$
	468.6	7.4(4)		−0.11(6)	+0.23(10)	$8^- \rightarrow 7^-$
	543.4	7.1(2)				$6^- \rightarrow 4^-$
	609.9	11.6(14)				$7^- \rightarrow 5^-$
	610.7	2.2(5)				$10^- \rightarrow 9^-$
	750.2	6.5(4)		+0.28(5)	−0.08(9)	$8^- \rightarrow 6^-$
	816.8	11.9(6)				$9^- \rightarrow 7^-$

(*continued on next page*)

Table 1 (*continued*)

	E_γ	Intensity[a]	$R_{\rm DCO}$[b]	$A_2/A_\circ$	$A_4/A_\circ$	Assignment[c]
	959.0	4.6(8)		+0.35(7)	−0.01(10)	$10^- \to 8^-$
	1027.4	7.8(5)		+0.35(7)	−0.15(11)	$11^- \to 9^-$
	1109.7	3.2(4)		+0.24(6)	−0.30(9)	$13^- \to 11^-$
	1173.7	2.6(4)				$(12^-) \to 10^-$
	1239.1	2.6(5)				$(15^-) \to 13^-$
	1348.3	1.5(2)				$(14^-) \to (12^-)$
	1407.9	0.9(3)				$(17^-) \to (15^-)$
	1530.2	0.6(3)				$(16^-) \to (14^-)$
Band 3 to Band 1	186.3	3.3(1)				$\to 5^-$
	232.4	2.1(8)				
	383.0	2.1(1)				$(6^+) \to$
	489.9	3.7(1)	$1.6(6)_{(D)}$	+0.24(3)	−0.03(7)	$(6^+) \to 6^-$
	553.0	4.7(2)		−0.15(4)	+0.10(12)	$(8^+) \to 7^-$
	720.1	5.3(8)				$(7^+) \to 6^-$
	802.1	45.5(50)	$0.5(1)_{(Q)}$	−0.28(8)	+0.16(13)	$(6^+) \to 5^-$
Band 3 to Band 4	114.1	1.0(4)				$(7^+) \to (6^+)$
	315.0	2.6(1)		+0.22(9)	+0.23(15)	$(8^+) \to (6^+)$
Band 3 to Band 5	304.7	1.2(1)	$0.5(3)_{(D)}$	+0.17(22)	−0.01(36)	$(8^+) \to (6^+)$
Band 4 to Band 3	474.2	3.8(14)		−0.93(6)	+0.21(9)	$(8^+) \to (7^+)$
Band 4 to Band 5	289.0	7.7(1)	$0.5(3)_{(Q)}$	−0.04(4)	+0.01(7)	$(6^+) \to (5^+)$
	527.1	5.6(2)		+0.25(10)	+0.05(16)	$(6^+) \to (4^+)$
	578.9	2.6(2)	$1.2(5)_{(D)}$			$(8^+) \to (6^+)$
Band 5 to Band 4	333.7	2.4(9)		−0.38(4)	+0.14(7)	$(7^+) \to (6^+)$

[a] The intensities of the low energy transitions are corrected for the internal conversion.
[b] The letters indexing the ratio values have the following meaning: (D) when the gate was set on dipole transition(s) and (Q) when the gate was set on quadrupole transition(s).
[c] See text and Fig. 3.

3. Discussion

The deformation of the ^{80}Y nucleus in the ground state and at low rotational frequencies has been discussed in detail in Refs. [6,7]. Total Routhian surfaces (TRS) calculated with the Hartree–Fock–Bogolyubov cranking model, based on a Woods–Saxon potential and a monopole pairing force, provide for different possible ground-state configurations a large prolate deformation, with $\beta_2 \approx 0.38$. This is comparable with the $\beta_2 = 0.43$ deformation predicted by the macroscopic–microscopic model used in Ref. [22]. The structure of the low-lying states in nearby odd-mass nuclei is dominated by the Nilsson orbitals $[422]5/2^+$, $[301]3/2^-$ and $[431]1/2^+$. The nucleus ^{81}Y has a $[422]5/2^+$ ground state and an isomeric $[301]3/2^-$ state at 113.4 keV [23,24]. The isotone of ^{80}Y, ^{79}Sr has a $[301]3/2^-$ ground state and an isomeric $[422]5/2^+$ state at 177.1 keV [25,26], as well as a low-lying $[431]1/2^+$ state [27]. On this basis, the 4^- ground state of ^{80}Y was assigned [6] as a coupling between the Nilsson orbitals $\pi[422]5/2^+$ and $\nu[301]/2^-$, according to the Gallagher–Moszkowski rule $I = \Omega_p + \Omega_n$ [28] (parallel coupling). In the same work [6], calculations have been performed with the two-quasiparticle + rotor model of

Ref. [29] assuming an axial-symmetric prolate shape and with the quadrupole deformation parameter ε_2 varied in the range from 0.35 to 0.43. The experimental excitation energies of the low-lying states have been reproduced well by inclusion of a spin-polarization term and a long-range force in the effective proton–neutron residual interaction. For a prolate deformation of the core $\varepsilon_2 \approx 0.38$ the dominating Nilsson configurations for the 4^- ground state and the 1^- isomeric state have been found to originate from the parallel and antiparallel coupling of the proton $[422]5/2^+$ and the neutron $[301]3/2^-$ orbitals. A second 1^- state originating from the coupling of the low-Ω proton $[431]1/2^+$ orbital with the neutron $[301]3/2^-$ orbital was also predicted at low energy. The 2^+ isomeric state has been described by the coupling of the proton $[422]5/2^+$ orbital with the low-Ω neutron $[431]1/2^+$ orbital which has significant amplitudes from the $d_{5/2}$ and $g_{7/2}$ subshells, while the lowest 5^+ state has been described by the $\pi[422]5/2^+ \otimes \nu[422]5/2^+$ configuration with $K = 5$. In the following the observed band structures at low spin will be discussed in the frame of the interacting boson–fermion–fermion model, which may be considered an alternative to the two-quasiparticle + rotor model. Then, the cranking formalism will be applied in order to describe the band properties at both low and higher spins.

3.1. Low-spin states and IBFFM description

The interacting boson–fermion–fermion model is the extension to odd–odd nuclei of the interacting boson model (IBM) [30] (for the even–even nuclei) and the interacting boson–fermion model (IBFM) [31] (for the odd-mass nuclei). The IBFFM Hamiltonian can be written as follows [32]:

$$H = H_{\mathrm{IBM}} + H_\pi + H_\nu + H_{\mathrm{B}\pi} + H_{\mathrm{B}\nu} + H_{\pi\nu}. \tag{1}$$

Here, H_{IBM} represents the usual IBM Hamiltonian for the even–even core [30], $H_{\pi(\nu)}$ describe the fermion single-particle interaction, while $H_{\mathrm{B}\pi(\mathrm{B}\nu)}$ describe the boson–fermion interactions. Equation (1) can be rewritten as $H = H_{\mathrm{IBFM}(\nu)} + H_{\mathrm{IBFM}(\pi)} - H_{\mathrm{IBM}} + H_{\pi\nu}$, where $H_{\mathrm{IBFM}(\nu,\pi)}$ represent the IBFM Hamiltonians [31] for the odd-mass nuclei. The last term is a neutron–proton residual interaction.

In this model, the ^{80}Y nucleus is described as two fermions (one proton fermion and one neutron-hole fermion) coupled to a ^{80}Sr core. Only two-qp states will be described within this model. In the first steps, the phenomenological parameters entering the first five terms of Eq. (1) must be determined by describing the properties of the ^{80}Sr core nucleus, and of the two adjacent odd-mass nuclei ^{81}Y and ^{79}Sr. Then, the Hamiltonian (1) will be diagonalized in a (truncated) space made by coupling proton and neutron states to the boson core space. For the Sr core we used the IBM parameters determined in Ref. [33]. For the description of the positive-parity states in ^{81}Y we used the IBFM parameters determined for the odd-mass Y isotopes in Ref. [34]. In these calculations, the odd proton was allowed to occupy the spherical shell model orbitals $1g_{9/2}$ and $2d_{5/2}$. Full details are given in Refs. [33,34]. Both positive and negative-parity states have then been calculated for ^{79}Sr, in a similar way to the calculations described in [34]. For the negative-parity states, the odd fermion was allowed to occupy the spherical orbitals $1f_{5/2}, 2p_{3/2}$ and $2p_{1/2}$. The parameters of the boson–fermion interaction terms were $A_0 = -0.1$, $\Gamma_0 = 0.3$, and $\Lambda_0 = 8.0$ MeV^2, while for the negative-parity states they had the values -0.1, 0.05

and 8.0, respectively (these parameters determine the strengths of the so-called monopole–monopole, quadrupole–quadrupole and exchange terms of the boson–fermion interaction, respectively [31]). The calculations of the energy levels and electromagnetic decay rates have been made with the codes PHINT and FBEM [35], and ODDA and PBEM [36], for the even–even and odd-mass nuclei, respectively. The calculations for the odd–odd nucleus have been performed with an IBFFM code written by Scholten [37]. This programme has been described in Ref. [38], and we refer to this work for the details concerning the way the diagonalization of the Hamiltonian (1) is made. In this code, the neutron–proton residual interaction consists of a quadrupole–quadrupole and a spin–spin term:

$$H_{\pi\nu} = V_q Q_\pi \cdot Q_\nu + V_s \sigma_\pi \cdot \sigma_\nu. \tag{2}$$

Positive-parity states in ^{80}Y have been calculated by allowing positive-parity configurations in both related odd-mass nuclei, while for the negative-parity ones we considered positive-parity configurations in ^{81}Y and negative-parity configurations in ^{79}Sr. The other two possible combinations, involving negative-parity configurations in ^{81}Y were not investigated, as they are expected to contribute to higher excitation energies. B(E2) transition

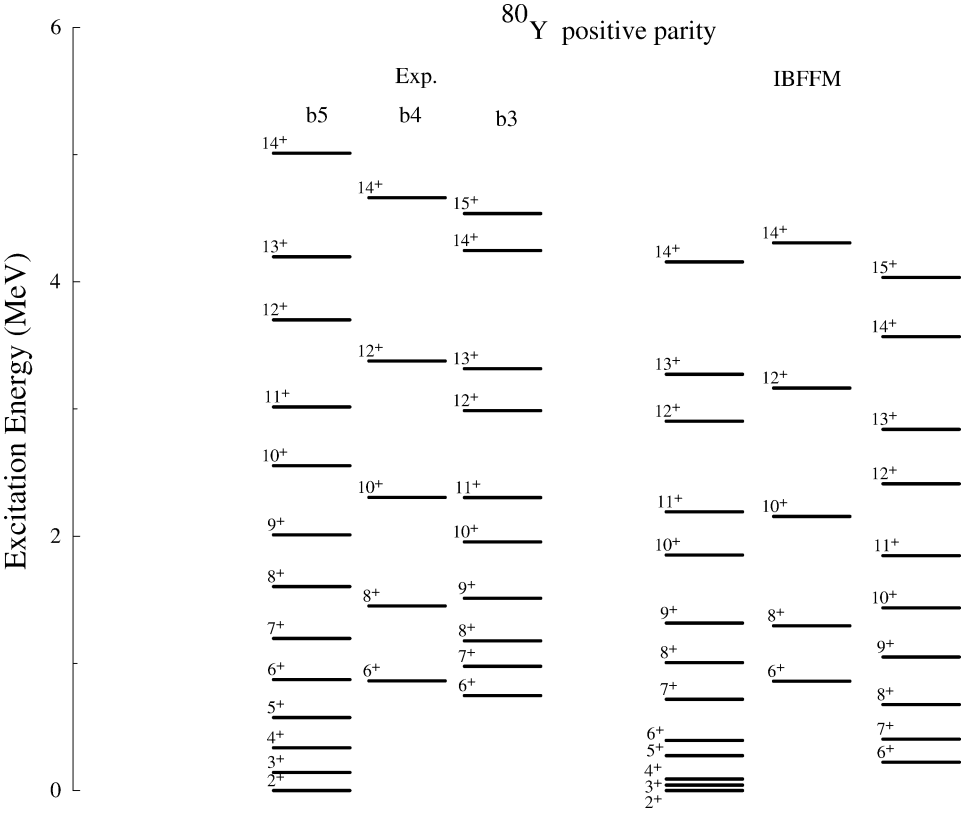

Fig. 6. Comparison between the IBFFM predictions and experiment for the positive-parity states (see text). Calculated branching ratios and the assignments of theoretical states to the experimental ones are given in Table 2.

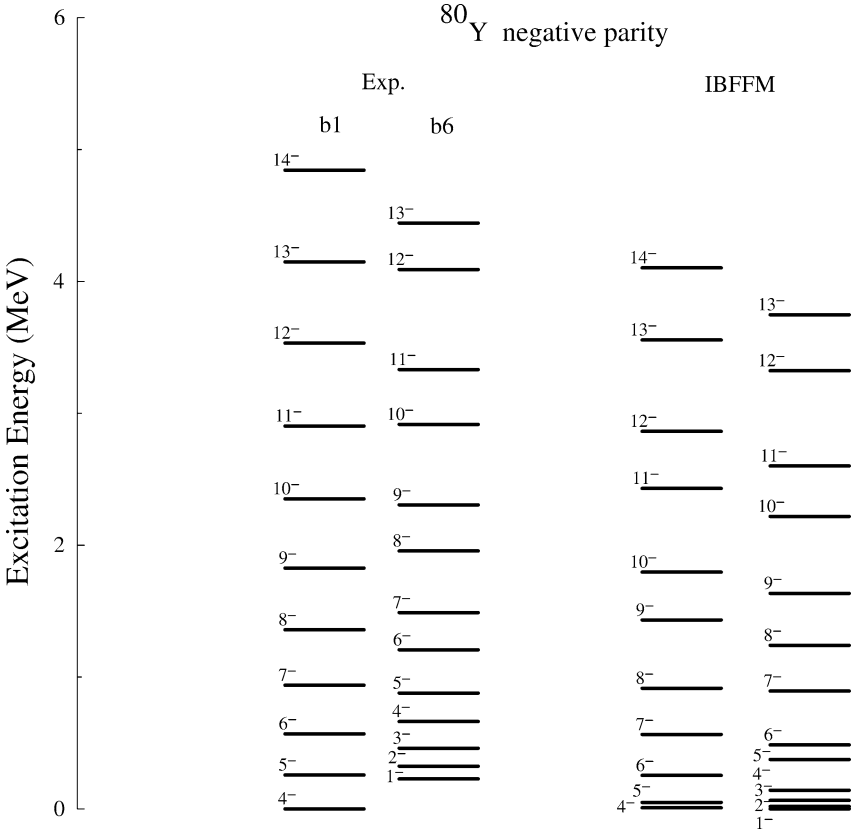

Fig. 7. Same as Fig. 6, but for the negative-parity states.

rates have been calculated with an operator which was chosen identical to that used in describing the E2 properties of the even–even core and the two related odd-mass nuclei, while the M1 properties used an operator similar to that for the odd-mass nuclei [38].

After having determined the IB(F)M parameters for both the core and odd-mass nuclei, the calculations for the odd–odd nucleus were straightforward, only the two parameters of the neutron–proton interaction having to be chosen. The quadrupole–quadrupole interaction was found to have very little effect on the results, and has been finally neglected. This is understandable, since most of the quadrupole interactions have already been taken care of by the boson–fermion interaction. The spin–spin interaction has effects on the ordering of the lowest states but a compromise for the description of both the positive and negative states required very small values for V_s, which did not influence so much the final results either, so we present below results obtained with a value $V_s = 0.03$ MeV.

Figures 6 and 7 show the results of the calculations for the positive-parity states (up to spin 14) and negative-parity states (up to spin 15), respectively. The calculated states have been arranged into bands which are tentatively associated to the experimental ones. The assignment of the calculated states to the observed ones has been made on the basis of

Table 2
Comparison between experimental and calculated (IBFFM) branching ratios in ^{80}Y. The first part of the table presents the in-band transitions, the second one the connections between the lowest states of the positive-parity bands. For each level, the strongest branch is normalized to 100

	Initial		Final		E_γ (keV)	Assignment		Branch	
	E_x(keV)	J_i^π	E_x(keV)	J_f^π		J_i^π	J_f^π	Calc.	Exp.
Band 1	570	6^-	257	5^-	313	6_1^-	5_1^-	26.6	100(3)
			0	4^-	570		4_1^-	100	38.9(44)
	938	7^-	570	6^-	368	7_1^-	6_1^-	16.0	8.9(34)
			257	5^-	681		5_1^-	100	100(2)
	1358	8^-	938	7^-	421	8_1^-	7_1^-	22.7	13.2(18)
			570	6^-	788		6_1^-	100	100(5)
	1826	9^-	1358	8^-	467	9_1^-	8_1^-	4.4	6.0(19)
			938	7^-	888		7_1^-	100	100(3)
	2350	10^-	1826	9^-	526	10_1^-	9_1^-	3.8	2.5(5)
			1358	8^-	992		8_1^-	100	100(7)
	2902	11^-	2350	10^-	552	11_1^-	10_1^-	1.5	–
			1358	8^-	992		8_1^-	100	100
Band 6	460	3^-	324	2^-	136	3_1^-	2_1^-	100	100(9)
			228	1^-	232		1_1^-	10.7	6.6(25)
	664	4^-	460	3^-	203	4_2^-	3_1^-	100	100(5)
			324	2^-	340		2_1^-	18.1	9.9(11)
	878	5^-	664	4^-	215	5_3^-	4_2^-	100	100(6)
			460	3^-	418		3_1^-	38.1	30.0(17)
	1207	6^-	878	5^-	328	6_2^-	5_3^-	77.6	100(8)
			664	4^-	543		4_2^-	100	40.1(11)
	1488	7^-	1207	6^-	282	7_2^-	6_2^-	92.7	100(9)
			878	5^-	610		5_3^-	100	20.2(46)
	1957	8^-	1488	7^-	469	8_2^-	7_2^-	5.9	100(5)
			1207	6^-	750		6_2^-	100	87.8(54)
	2305	9^-	1957	8^-	348	9_2^-	8_2^-	23.7	27.7(34)
			1488	7^-	817		7_2^-	100	100(5)
	2916	10^-	2305	9^-	611	10_2^-	9_2^-	1.0	48(11)
			1957	8^-	959		8_2^-	100	100(17)
	3332	11^-	2916	10^-	416	11_2^-	10_2^-	4.3	–
			2305	9^-	1027		9_2^-	100	100
Band 3	1490	(8^+)	1290	(7^+)	200	8_1^+	7_1^+	9.9	24.2(25)
			1059	(6^+)	431		6_1^+	100	100(2)
	1824	(9^+)	1490	(8^+)	334	9_1^+	8_1^+	31.0	100(6)
			1290	(7^+)	534		7_1^+	100	25.4(24)
	2267	(10^+)	1824	(9^+)	444	10_1^+	9_1^+	5.9	10.6(16)
			1490	(8^+)	777		8_1^+	100	100(3)
	2616	(11^+)	2267	(10^+)	348	11_1^+	10_1^+	3.0	32.2(28)
			1824	(9^+)	792		9_1^+	100	100(24)
	3298	(12^+)	2616	(11^+)	683	12_1^+	11_1^+	3.2	6.0(18)
			2267	(10^+)	1031		10_1^+	100	100(23)

Table 2 (*continued*)

	Initial		Final		E_γ (keV)	Assignment		Branch	
	E_x(keV)	J_i^π	E_x(keV)	J_f^π		J_i^π	J_f^π	Calc.	Exp.
	3629	(13^+)	3298	(12^+)	330	13_1^+	12_1^+	0.5	7.7(18)
			2616	(11^+)	1013		11_1^+	100	100(24)
	4558	(14^+)	3629	(13^+)	929	14_1^+	13_1^+	1.9	–
			3298	(12^+)	1260		12_1^+	100	100
Band 5	648	(4^+)	455	(3^+)	193	4_1^+	3_1^+	100	100(5)
			312	(2^+)	336		2_1^+	4.1	3.0(4)
	886	(5^+)	648	(4^+)	238	5_2^+	4_1^+	100	100(20)
			455	(3^+)	431		3_1^+	13.1	40.8(14)
	1185	(6^+)	886	(5^+)	299	6_2^+	5_2^+	100	100(2)
			648	(4^+)	537		4_1^+	14.1	50.7(16)
	1509	(7^+)	1185	(6^+)	324	7_2^+	6_2^+	100	55.5(16)
			886	(5^+)	623		5_2^+	18.3	100(21)
	1915	(8^+)	1509	(7^+)	407	8_2^+	7_2^+	78.6	100(3)
			1185	(6^+)	730		6_2^+	100	93.5(3)
	2323	(9^+)	1915	(8^+)	407	9_2^+	8_2^+	100	39(12)
			1509	(7^+)	814		7_2^+	63.1	100(39)
	2866	(10^+)	2323	(9^+)	544	10_2^+	9_2^+	5.8	15.8(53)
			1915	(8^+)	951		8_2^+	100	100(32)
	3328	(11^+)	2866	(10^+)	461	11_2^+	10_2^+	19.3	23.1(51)
			2323	(9^+)	1005		9_2^+	100	100(8)
	4013	(12^+)	3328	(11^+)	685	12_2^+	11_2^+	1.2	21(10)
			2866	(10^+)	1147		10_2^+	100	100(17)
	4509	(13^+)	4013	(12^+)	496	13_2^+	12_2^+	2.5	–
			3328	(11^+)	1181		11_2^+	100	100
Levels with branches out of band									
	1185	(6^+)	1059	(6^+)	126	6_2^+	6_1^+	0.02	–
			886	(5^+)	299		5_2^+	100	100(2)
			648	(4^+)	537		4_1^+	14.1	50.7(16)
	1509	(7^+)	1290	(7^+)	219	7_2^+	7_2^+	0.1	–
			1059	(6^+)	450		6_1^+	0.1	–
			1185	(6^+)	324		6_2^+	100	55.5(16)
			1175	(6^+)	334		6_3^+	0.1	–
			886	(5^+)	623		5_2^+	18.3	100(21)
	1490	(8^+)	1059	(6^+)	431	8_1^+	6_1^+	100	100(2)
			1185	(6^+)	305		6_2^+	0.6	3.3(3)
			1175	(6^+)	315		6_3^+	0.03	7.2(3)
			1290	(7^+)	200		7_1^+	9.9	24.2(25)
	1290	(7^+)	1059	(6^+)	231	7_1^+	6_1^+	21.1	100(4)
			1185	(6^+)	105		6_2^+	4.9	–
			1175	(6^+)	115		6_3^+	100	6.8(27)
			886	(5^+)	404		5_2^+	0.3	–

(*continued on next page*)

Table 2 (*continued*)

Initial		Final		E_γ (keV)	Assignment		Branch	
E_x(keV)	J_i^π	E_x(keV)	J_f^π		J_i^π	J_f^π	Calc.	Exp.
1175	(6^+)	1059	(6^+)	116	6_3^+	6_1^+	1.3	–
		886	(5^+)	289		5_2^+	100	100(1)
		648	(4^+)	527		4_1^+	0.01	73(3)
1764	(8^+)	1490	8^+	274	8_3^+	8_1^+	8.5	–
		1290	(7^+)	474		7_1^+	14.9	73(27)
		1509	(7^+)	255		7_2^+	63.3	–
		1059	(6^+)	705		6_1^+	100	–
		1185	(6^+)	579		6_2^+	2.1	50(4)
		1175	(6^+)	589		6_3^+	10.6	100(4)

their decay modes. The calculated branching ratios are compared to the experimental ones in Table 2, where it can be seen that the calculations describe reasonably well the data. As seen in Table 2, the 5^+ state from band 5 has been assigned as the second calculated (5_2^+) state. The calculated 5_1^+ state might be associated with the state lying just below the 6^+ state of band 3. The three states placed below this 6^+ state are fed by the weak transitions of 383, 232 and 186 keV, and could not be well characterized, even their order being somewhat doubtful (Table 1). Assuming, nevertheless, that the state at 675 keV (to which the 1059 keV, 6^+ state decays through the 383 keV transition) is the 5_1^+ state, then it is found that the 6_1^+ state decays predominantly to this state, while the 7_2^+ and 6_2^+ states (from band 5) have very weak branches towards this state (compared with those to other states, shown in Table 2), as is observed experimentally.

The IBFFM wave-functions for the positive-parity states are dominated by the $g_{9/2}$ proton and neutron orbitals, while in the negative-parity states the dominating orbitals are $\pi g_{9/2}$ and $\nu f_{5/2}$. In some cases, this confirms the Nilsson assignments made on the basis of the two-qp-plus-rotor model. On the other hand, the present calculations cannot provide a strong contribution of the $d_{5/2}$ orbital to the wave-functions. The spherical $d_{5/2}$ orbital is rather distant with respect to the $g_{9/2}$ one, therefore it comes into the wave-functions of the odd-A isotopes with contributions smaller than 10%. Therefore, we do not expect a very good description of the well deformed case, when the [431]1/2 orbital (of $d_{5/2}$ origin) comes very strongly into competition. Fig. 8 shows how the $B(\mathrm{M1})/B(\mathrm{E2})$ ratio is predicted for the assigned bands. This quantity is predicted too strong by a factor of 3–4 at the lower spins in band 5, and is somewhat underestimated for band 6, for both these bands the estimated contribution of the [431]1/2 orbital being rather important (see the CSM discussion below). The $B(\mathrm{M1})$ strengths are also predicted too small for the odd-spin members of the positive-parity band 3 (as also visible in the predicted branching ratios, Table 2).

Another shortcoming of these calculations appears to be the inability to accurately describe the relative positions of the band-heads and the spacings of the lowest states in the bands. Better relative positions of the negative and positive-parity band-heads would have required different values of V_s. On the other hand, although one could improve a little

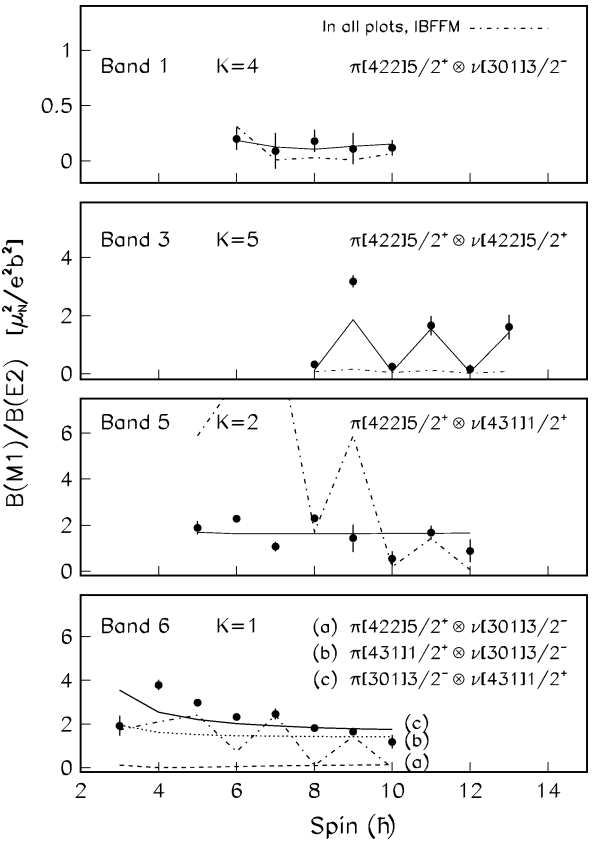

Fig. 8. Experimental and calculated $B(\mathrm{M1})/B(\mathrm{E2})$ values for the bands in ^{80}Y. For all bands, the IBFFM predictions are shown by the dash-dotted line, while the other curves are calculated with the CSM for the indicated configurations.

also the spacings of the lowest states, this had very little effect on the calculated decay properties. These shortcomings may be attributed to the inadequacy of the neutron–proton interaction used. The importance of this interaction in describing details of the observed level scheme was emphasized both in the two-qp-plus-rotor model [6] and in the case of other IBFFM calculations. Especially, in the IBFFM calculations, better results are obtained when using a surface-δ interaction [32]. Since the code we used had only the interaction (2), we could not check such effects.

We checked further our IBFFM calculations for the $g_{9/2} \otimes g_{9/2}$ band which was observed also in the heavier odd–odd Y isotopes, ^{82}Y [17–19] and ^{84}Y [20,21]. Fig. 9 shows the way this band is described also in ^{82}Y and ^{84}Y, by calculations similar to those described above for ^{80}Y. The main features of the bands are well described up to the backbending (crossing with other bands, see below). Although not in perfect phase with the observed one, the calculations also show an inversion of the signature splitting

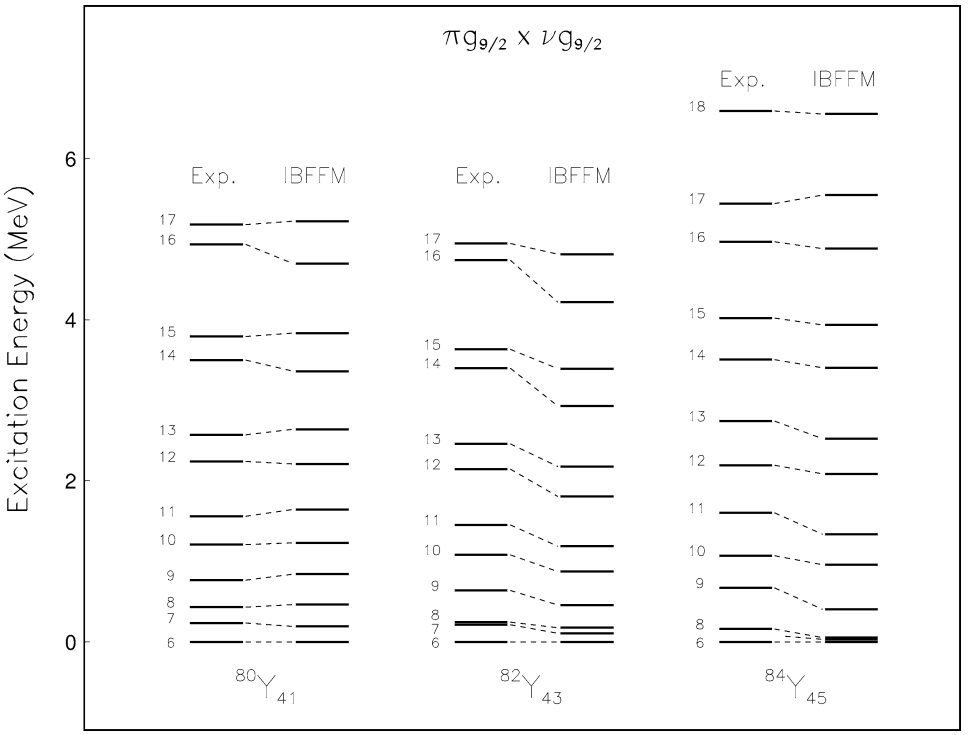

Fig. 9. Comparison experiment—IBFFM predictions for the positive-parity band 5 (Fig. 3) and its analogues in ^{82}Y [17–19] and ^{84}Y [20,21].

at low spins, and at higher spins (above $9\,\hbar$ for the lighter isotopes, and $11\,\hbar$ for ^{84}Y) the signature splitting is well described.

3.2. Cranked shell-model interpretation

The cranking formalism outlined in Ref. [39] has been applied to transform the experimental excitation energies and spins of the bands into Routhians, alignments and kinematic and dynamic moments of inertia as a function of rotational frequency ω. These quantities are plotted in Fig. 10. The Routhians and angular momentum alignments have been calculated by using a Harris reference with the parameters $J_0 = 16\hbar^2/\mathrm{MeV}$ and $J_1 = 1\,\hbar^4/\mathrm{MeV}^3$, as used in other nuclei from this mass region (e.g., ^{81}Y [24]). Another quantity which shows the degree of signature splitting without the need of considering a reference configuration is $(E(I) - E(I-1))/2I$. This expression is illustrated as a function of I for the bands observed in ^{80}Y in the right side of Fig. 11. In the left side of the figure the signature splitting index for band 5 is compared with that of the similar bands from from ^{82}Y [17–19] and ^{84}Y [20,21]. A perfect rotor has no signature splitting, in which case this quantity is constant and equal to $\hbar^2/2\Im$, while when a signature splitting is present this gives rise to an alternating pattern. All bands have a "normal" signature splitting at higher spins, that is, $\alpha = 1$ is the favoured signature, as expected [40], based on the particle

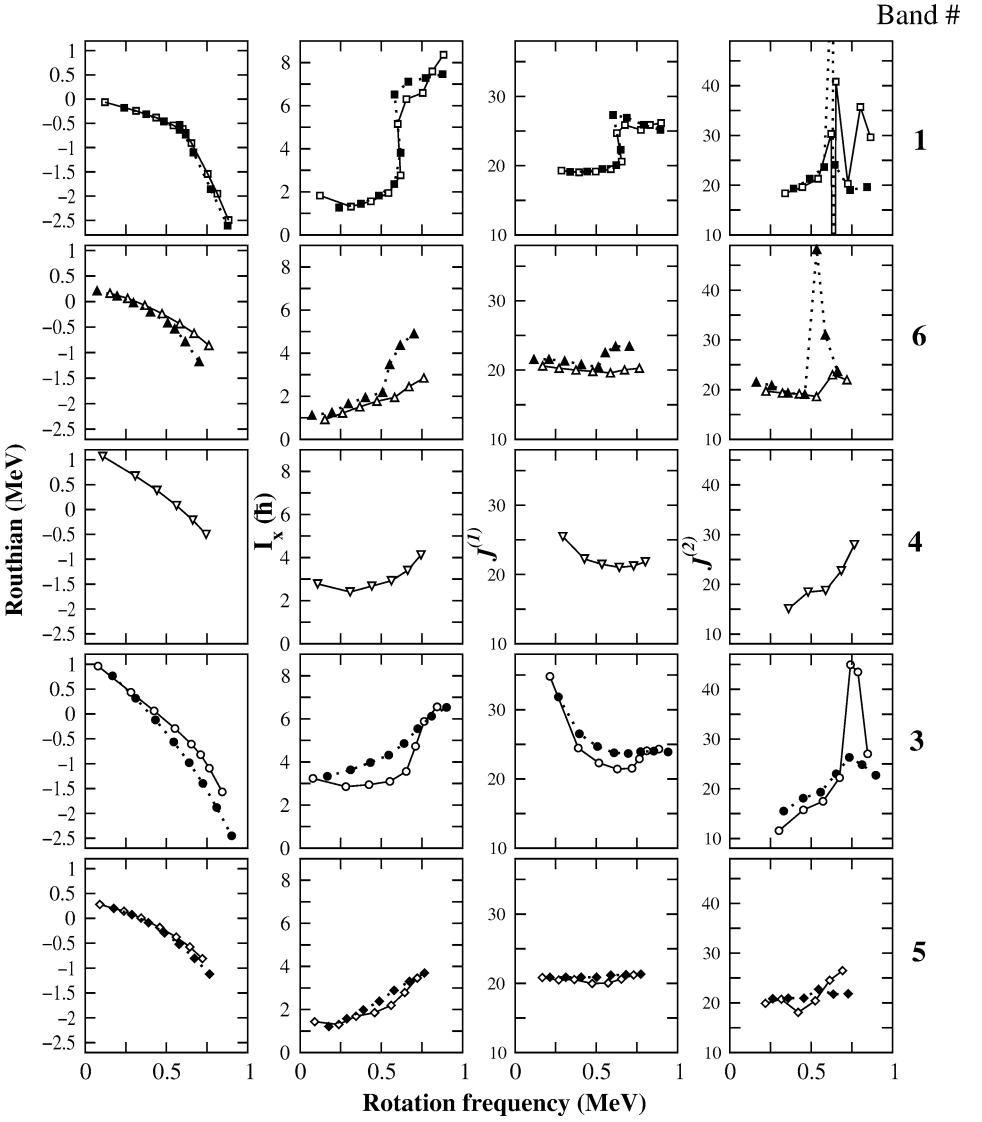

Fig. 10. Experimental Routhians, angular momentum alignments, kinematic moments of inertia, and dynamic moments of inertia for the bands observed in ^{80}Y (as numbered in Fig. 3). A Harris reference with the parameters $J_0 = 16\hbar^2/\text{MeV}$ and $J_1 = 1\hbar^4/\text{MeV}^3$ has been used. Empty symbols represent signature $\alpha = 0$, filled symbols $\alpha = 1$.

configurations discussed in the preceding subsection. One can see that bands 1, 5 and 6 start with a rather small signature splitting, therefore have a good rotational behaviour. Changes of the pattern of the signature splitting index, like, e.g., increase or decrease of its oscillation magnitude, indicate structure changes, and can be corroborated with changes in Routhians, alignments, and moments of inertia.

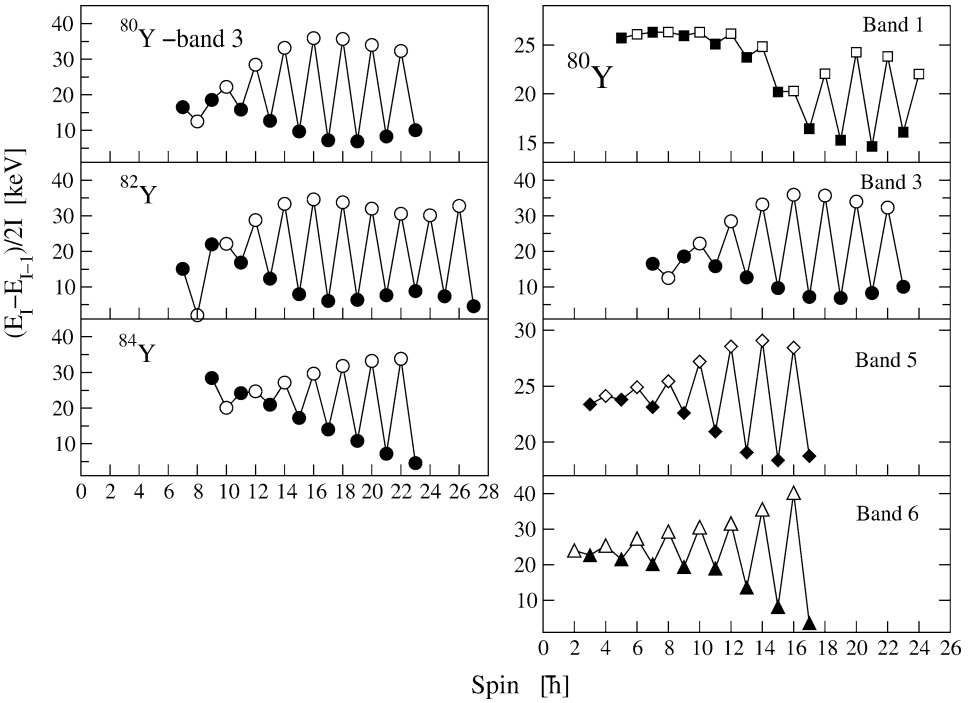

Fig. 11. Signature splitting index for the different bands observed in ^{80}Y. The left panel compares this quantity for band 5 with that of the similar bands from ^{82}Y [17–19] and ^{84}Y [20,21]. Meaning of empty and filled symbols as in Fig. 10.

Valuable information about the intrinsic structure of the bands has been provided by the analysis of the $B(\mathrm{M1})/B(\mathrm{E2})$ ratios. The experimental ratios have been derived from the gamma-ray branching ratios using the relation:

$$\frac{B(\mathrm{M1}, I \to I-1)}{B(\mathrm{E2}, I \to I-2)} = 0.6967 \frac{E_\gamma^5(I \to I-2)}{E_\gamma^3(I \to I-1)} \frac{1}{\lambda(1+\delta^2)} \left[\frac{\mu_N^2}{e^2\,\mathrm{mb}^2}\right], \tag{3}$$

where the gamma-ray energies E_γ are given in MeV, $\lambda = I_\gamma(I \to I-2)/I_\gamma(I \to I-1)$ is the branching ratio and δ is the E2/M1 mixing ratio. In the present case mixing ratios were not determined experimentally. We have therefore evaluated them from the measured branching ratios using the rotational model relation [41], assuming pure K-value:

$$\frac{1}{\delta^2} = \frac{1}{\lambda} \frac{E_\gamma^5(I \to I-2)}{E_\gamma^5(I \to I-1)} \frac{\langle IK20|I-2K\rangle^2}{\langle IK20|I-1K\rangle^2} - 1. \tag{4}$$

Rather large values for the mixing ratios ($\delta^2 > 0.5$) have been calculated for the dipole transitions in band 1. In the other bands the correction for the mixing ratios was found to be negligibly small.

The experimental $B(\mathrm{M1}, I \to I-1)/B(\mathrm{E2}, I \to I-2)$ ratios are illustrated in Fig. 8 together with calculated values for appropriate configurations. In the theoretical estimates

a generalization of the semi-classical formula [42] for the $B(\mathrm{M1}, I \to I-1)$ value has been used:

$$B(\mathrm{M1}, I \to I-1) = \frac{3}{8\pi I^2}\Bigg[(g_{\Omega_p} - g_R)\big\{\Omega_p\sqrt{I^2-K^2} - i_p K\big\} + (g_{\Omega_n} - g_R)\Bigg\{\Omega_n\sqrt{I^2-K^2}\left(1 \pm \frac{\Delta e}{\hbar\omega}\right) - i_n K\Bigg\}\Bigg]^2 \big(\mu_N^2\big). \tag{5}$$

g_{Ω_p}, g_{Ω_n}, and g_R are the proton, neutron and collective g factors, respectively. The quantities i_p and i_n represent the aligned angular momenta of the proton and the neutron, respectively. Values of 1.5, 0 and 2 have been considered for the $[422]5/2^+$, $[301]3/2^-$ and $[431]1/2^+$ orbitals, respectively, based on experimental alignment observed in neighbouring odd-mass nuclei. Δe is the signature splitting in the level energies in the rotating frame. A staggering effect on the $B(\mathrm{M1})/B(\mathrm{E2})$ ratios was observed in band 3 and was attributed to the neutron $[422]5/2^+$ orbital. The proton and neutron g_Ω factors were calculated as:

$$g_\Omega = \frac{1}{\Omega}\big[g_l\langle l_3\rangle + g_s\langle s_3\rangle\big], \tag{6}$$

assuming 70% of the free nucleon g_s factors ($g_s^{\mathrm{free}} = 5.59$ for proton and -3.83 for neutrons). The expectation values of the spin projection on the symmetry axis, $\langle s_3\rangle$, were evaluated using Nilsson type wave functions obtained from the diagonalization of the deformed harmonic oscillator with $\varepsilon_2 = 0.36$, which corresponds to a deformation $\beta_2 = 0.38$. The $\langle s_3\rangle$ and g_Ω values are summarized in Table 3. In the same table are also presented g_Ω factors deduced from experimental g factors of low-lying states in neighbouring odd-mass nuclei by using the expression:

$$g = g_R + (g_\Omega - g_R)\frac{\Omega^2}{I(I+1)}. \tag{7}$$

The empirical g_Ω values agree within errors with the theoretical g_Ω and were used in the $B(\mathrm{M1})/B(\mathrm{E2})$ calculations whenever available.

Table 3
Calculated and empirical g_Ω for proton and neutron single-particle states considered for ^{80}Y

Proton	$\langle s_z\rangle$	g_Ω^{cal}	g_Ω^{emp}	Neutron	$\langle s_z\rangle$	g_Ω^{cal}	g_Ω^{emp}
$[422]\frac{5}{2}^+$	+0.40	1.47	1.70(14)	$[422]\frac{5}{2}^+$	+0.40	−0.43	−0.39(5)
$[301]\frac{3}{2}^-$	−0.40	1.78	1.97(24)	$[301]\frac{3}{2}^-$	−0.36	−0.64	−0.85(10)
$[431]\frac{1}{2}^+$	−0.12	0.30	–	$[431]\frac{1}{2}^+$	−0.06	+0.32	–

The expectation values $\langle s_3\rangle$ have been obtained within the framework of the Nilsson model using the deformation parameter of $\varepsilon_2 = 0.36$. The values of g_Ω^{cal} were deduced by Eq. (6) assuming 70% of the free nucleon g_s factors. The values of g_Ω^{emp} were derived by Eq. (7) using $g_R = 0.48(5)$ and experimental g factors as follows: $g(5/2^+, {}^{79}\mathrm{Rb}) = 1.343(1)$, $g(5/2^+, {}^{77}\mathrm{Sr}) = -0.140(2)$, $g(3/2^-, {}^{81}\mathrm{Rb}) = 1.373(1)$, $g(3/2^-, {}^{79}\mathrm{Sr}) = -0.316(1)(1)$ [43].

The values of the $B(\mathrm{E2}, I \to I-2)$ were calculated according to the expression:

$$B(\mathrm{E2}, I \to I-2) = \frac{5}{16\pi} Q_\circ^2 \langle I\,K\,20|I-2\,K\rangle^2 \left(e^2\,\mathrm{b}^2\right). \tag{8}$$

An intrinsic quadrupole moment $Q_\circ = 3.2\ e\,\mathrm{b}$, corresponding to $\beta_2 = 0.38$, has been adopted in the calculations.

In the following we shall discuss each band in connection with the quantities shown in Figs. 8, 10 and 11.

3.2.1. Band 1

The configuration $\pi[422]5/2^+ \otimes \nu[301]3/2^-$ assigned in Ref. [6] to the 4^- bandhead is supported by the observed electromagnetic properties of the band. As seen in Fig. 8, small values were determined experimentally for the $B(\mathrm{M1})/B(\mathrm{E2})$ ratios, which are in good accordance with the calculated values for the assigned configuration, as well as with those calculated by the IBFFM. At low frequencies the band has no signature splitting. A first particle alignment within this band takes place at a rotational frequency $\hbar\omega \approx 0.64$ MeV, as shown by the sharp increase in the angular momentum alignment and in the kinematic moment of inertia or the very irregular behaviour of the dynamic moment of inertia for both signatures. This alignment must be due to a $g_{9/2}$ neutron pair since the proton $g_{9/2}$ orbital is blocked. Indeed, its rotational frequency almost coincides with that of the first alignment observed in ^{81}Y (at 0.67 MeV), which has a similar deformation [24] and is also accompanied by a large gain in alignment, of about $5.5\,\hbar$. One notices that above the alignment the band shows an increase of the signature splitting, which further confirms the $g_{9/2}$ neutron alignment, as this orbital is known to have an oblate deformation and large signature splitting in the odd-N neighbouring nuclei [26,44]. A second alignment may be at $\hbar\omega \approx 0.82$ MeV, as seen from the further increase of the alignment for the $\alpha = 0$ signature, or the second peak in the dynamic moment of inertia. The second alignment may be assigned to the breaking of a proton $g_{9/2}$ pair which is also observed in ^{81}Y at 0.74 MeV [24] and in the ^{80}Sr core at 0.75 MeV [45]. The $g_{9/2}$ proton alignment would drive the nucleus back to a prolate shape and give rise to decreased signature splitting. This interpretation is in accordance with the experimental signature splitting which shows a tendency to decrease at the highest spins (see Fig. 11).

3.2.2. Band 2

Only one signature was observed for this band. Furthermore, it is not so well characterized experimentally, therefore it is difficult to attempt any configuration assignment. However, this apparent forking of the negative-parity band 1 above the 13^- state is rather intriguing.

3.2.3. Band 3

This band shows a distinct signature splitting, which is consistent with its assigned configuration $\pi[422]5/2^+ \otimes \nu[422]5/2^+$. As seen in Fig. 11, the signature splitting shows an inversion of sign at spin 9, similar to the one observed in ^{82}Y [17,18] and ^{84}Y [20,21]. This has been interpreted as a change from the regime with excitation modes based on both quasiparticle alignments and rotation, to one based only on rotation (at higher spins).

The $B(\mathrm{M1})/B(\mathrm{E2})$ ratios also present a staggering, which is well accounted for (Fig. 8) by the cranking calculations in which an average signature splitting of $\Delta e = 0.2$ MeV at $\hbar\omega = 0.4$ MeV has been used. Both signatures show a crossing at $\hbar\omega \approx 0.77$ MeV, which is rather broad for the $\alpha = 1$ signature and could be assigned to the $g_{9/2}$ proton alignment. The observed decrease in the signature splitting beyond spin 19 (Fig. 11) may indicate a change in shape due to this quasiparticle alignment.

3.2.4. Band 4

This band formed by a sequence of E2 transitions has been assigned as having mainly a $g_{9/2} \otimes g_{9/2}$ structure, on the basis of the IBFFM calculations. At low energies there are direct connections of this band with bands 3 and 5, suggesting similarities in their structures. The observed signature ($\alpha = 0$) of this band shows a rather gradual alignment which peaks around 0.75 MeV or even later, indicating a possible band crossing with large interaction, due to the $g_{9/2}$ proton alignment.

3.2.5. Band 5

The 2^+ band-head has been described within the two-quasiparticle + rotor model by the $\pi[422]5/2^+ \otimes \nu[431]1/2^+$ configuration [6]. The experimental $B(\mathrm{M1})/B(\mathrm{E2})$ ratios are in agreement with calculated values for this configuration (see Fig. 8). This band has no signature splitting and rather constant and almost equal kinematic and dynamic moments of inertia, which indicates rigid rotation. The presence of the neutron $[431]1/2^+$ intruder orbital in the structure of the neutron deficient nuclei with $A \approx 80$ was suggested in [46–48] to explain the strongly deformed $K^\pi = 1/2^+$ band observed in ^{81}Sr. We note that the dynamical moments of inertia in that band [48] are similar to those of band 5 in ^{80}Y, which gives further support to the assigned configuration. The broad alignment observed above 0.5 MeV is accompanied by an increased signature splitting (see Fig. 10). This indicates the alignment of a pair of $g_{9/2}$ neutrons driving the nucleus to an oblate shape.

3.2.6. Band 6

The band-head has been interpreted [6] as resulting from the antiparallel coupling of the proton $[422]5/2^+$ and neutron $[301]3/2^-$ orbitals. The calculated $B(\mathrm{M1})/B(\mathrm{E2})$ for this configuration are however very small, in disagreement with experimental values, as shown in Fig. 8, while the IBFFM values also generally underestimate the data. As already mentioned, the $K = 1$ band could result also from the coupling of the low-Ω $[431]1/2^+$ orbital with the $[301]3/2^-$ orbital. Calculated $B(\mathrm{M1})/B(\mathrm{E2})$ for the two possible configurations of this type $\pi[431]1/2^+ \otimes \nu[301]3/2^-$ and $\pi[301]3/2^- \otimes \nu[431]1/2^+$, respectively, are much closer to the experimental values (see Fig. 11). Consequently, this band may have a more complicated mixing from several Nilsson orbitals. The band has only one crossing in the investigated domain of frequencies, which shows up clearly in the $\alpha = 1$ signature at $\hbar\omega \approx 0.53$ MeV, and somewhat attenuated and more delayed (around 0.6 MeV) in the $\alpha = 0$ signature. The increased signature splitting at high spins suggests again the alignment of a pair of $g_{9/2}$ neutrons.

4. Summary

High-spin states in the neutron-deficient nucleus ^{80}Y have been observed in heavy-ion fusion–evaporation reactions. The unambiguous assignment of prompt gamma rays to this nucleus has been made by measuring them in coincidence with both a recoil mass spectrometer and a charged particle Si ball. The previously published level scheme [4] has been extended with new bands and transitions. Several band structures with rotational characteristics have been observed up to spins of at least 17, indicating a nucleus with large quadrupole deformation. The observed band structures are discussed on the basis of the interacting boson–fermion–fermion model and of the cranked shell model, thus allowing assignments of their main configuration. Measurements of absolute electromagnetic decay transition probabilities (level lifetimes), which should be possible now with the largest Ge detector arrays, would be important to better characterize the structure of this nucleus, and the evolution of its shapes with the rotational frequency.

References

[1] W. Nazarewicz, J. Dudek, R. Bengtsson, T. Bengtsson, I. Ragnarsson, Nucl. Phys. A 435 (1985) 397.
[2] C.J. Lister, P.J. Ennis, A.A. Chishti, B.J. Varley, W. Gelletly, H.G. Price, A.N. James, Phys. Rev. C 42 (1990) 1191.
[3] C.J. Lister, M. Campbell, A.A. Chishti, W. Gelletly, L. Goettig, R. Moscrop, B.J. Varley, A.N. James, T. Morrison, H.G. Price, J. Simpson, K. Connel, O. Skeppstedt, Phys. Rev. Lett. 59 (1987) 1270.
[4] D. Bucurescu, C.A. Ur, D. Bazzacco, C. Rossi Alvarez, P. Spolaore, C.M. Petrache, M. Ionescu-Bujor, S. Lunardi, N.H. Medina, D.R. Napoli, M. De Poli, G. de Angelis, F. Brandolini, A. Gadea, P. Pavan, G.F. Segato, Z. Phys. A 352 (1995) 361.
[5] P.H. Regan, C. Chandler, C.J. Pearson, B. Blank, R. Grzywacz, M. Lewitowicz, A.M. Bruce, W.N. Catford, N. Curtis, S. Czajkowski, P. Dessagne, A. Fleury, W. Gelletly, J. Giovinazzo, Z. Janas, C. Longour, C. Marchand, C. Miehe, N.A. Orr, R.D. Page, M.S. Pravikoff, A.T. Reed, M.G. Saint-Laurent, S.M. Vincent, R. Wadsworth, D.D. Warner, J.S. Winfield, Acta Phys. Pol. B 28 (1997) 431.
[6] J. Döring, H. Schatz, A. Aprahamian, R.C. de Haan, J. Göres, M. Wiescher, W.B. Walters, J. Rikovska, L.T. Brown, C.N. Davids, C.J. Lister, D. Seweryniak, B. Foy, Phys. Rev. C 57 (1998) 1159.
[7] C. Chandler, P.H. Regan, B. Blank, C.J. Pearson, A.M. Bruce, W.N. Catford, N. Curtis, S. Czajkowski, Ph. Dessagne, A. Fleury, W. Gelletly, J. Giovinazzo, R. Grzywacz, Z. Janas, M. Lewitowicz, C. Marchand, Ch. Miehe, N.A. Orr, R.D. Page, M.S. Pravikoff, A.T. Reed, M.G. Saint-Laurent, S.M. Vincent, R. Wadsworth, D.D. Warner, J.S. Winfield, F. Xu, Phys. Rev. C 61 (2000) 044309.
[8] J.J. Ressler, W.B. Walters, R. Grzywacz, J.C. Batchelder, C.R. Bingham, C.J. Gross, Z. Janas, M. Lipoglavsek, J. McConnell, S.D. Paul, A. Piechaczek, K. Rykaczewski, D. Radford, J. Shergur, Phys. Rev. C 63 (2001) 067303.
[9] D. Bazzacco, in: Proc. Int. Conf. on Nuclear Structure at High Angular momentum, Ottawa, 1992, Vol. II, Report No. AECL 10613, p. 376.
[10] E. Farnea, G. de Angelis, M. De Poli, P. De Ačuna, A. Gadea, D.R. Napoli, P. Spolaore, A. Buscemi, R. Zanon, R. Isocrate, D. Bazzacco, C. Rossi Alvarez, P. Pavan, A.M. Bizzeti-Sona, P.G. Bizzeti, Nucl. Instrum. Methods Phys. Res. A 400 (1997) 87.
[11] P. Spolaore, D. Ackermann, P. Bednarczyk, G. De Angelis, D. Napoli, C. Rossi Alvarez, D. Bazzacco, R. Burch, L. Müller, G.F. Segato, F. Scarlassara, Nucl. Instrum. Methods Phys. Res. A 359 (1995) 500.
[12] C.J. Lister, P.E. Haustein, D.E. Alburger, J.W. Olness, Phys. Rev. C 24 (1981) 260.
[13] S. della Negra, H. Gauvin, D. Jacquet, Y. Le Beyec, Z. Phys. A 307 (1982) 305.
[14] J. Döring, A. Aprahamian, R.C. de Haan, J. Göres, H. Schatz, M. Wiescher, W.B. Walters, L.T. Brown, C.N. Davids, C.J. Lister, D. Seweryniak, Phys. Rev. C 59 (1999) 59.

[15] A. Piechaczek, E.F. Zganjar, J.C. Batchelder, C.R. Bingham, T.N. Ginter, C.J. Gross, R. Grzywacz, B.D. Macdonald, S.D. Paul, K. Rykaczewski, K.S. Toth, Phys. Rev. C 61 (2001) 047306.
[16] Yu.N. Novikov, H. Schatz, P. Dendooven, R. Béraud, Ch. Miehé, A.V. Popov, D.M. Seliverstov, G.K. Vorobjev, P. Baumann, M.J.G. Borge, G. Canchel, Ph. Desagne, A. Emsallem, W. Huang, J. Huikari, A. Jokinen, A. Knipper, V. Kolhinen, A. Nieminen, M. Oinonen, H. Pentillä, K. Peräjärvi, I. Piqueras, S. Rinta-Antila, J. Szerypo, Y. Wang, J. Äystö, Eur. Phys. J. A 11 (2001) 257.
[17] P.C. Womble, J. Döring, T. Glasmacher, J.C. Holcomb, G.D. Johns, T.D. Johnson, P.J. Petters, M.A. Riley, V.A. Wood, S.L. Tabor, Phys. Rev. C 47 (1993) 2546.
[18] S.D. Paul, H.C. Jain, S. Chattopadhyay, M.L. Jhingan, J.A. Sheikh, Phys. Rev. C 51 (1995) 2959.
[19] J. Mukai, A. Odahara, H. Tomura, S. Suematsu, S. Mitarai, T. Kuroyanagi, D. Jerrestam, J. Nyberg, G. Sletten, A. Atac, S.E. Arnell, H.A. Roth, Ö. Skeppstedt, Nucl. Phys. A 568 (1994) 202.
[20] S. Chattopadhyay, H.C. Jain, J.A. Sheikh, Y.K. Agarval, M.L. Jhingan, Phys. Rev. C 47 (1993) R1.
[21] S. Chattopadhyay, H.C. Jain, S.D. Paul, J.A. Sheikh, M.L. Jhingan, Phys. Rev. C 49 (1995) 116.
[22] P. Möller, J.R. Nix, W.D. Myers, W.J. Swiatecki, At. Data Nucl. Data Tables 59 (1995) 185.
[23] T.D. Johnson, A. Raguse, C.J. Gross, M.K. Kabadiyski, K.P. Lieb, D. Rudolph, M. Weiszflog, T. Burkardt, J. Eberth, S. Skoda, Z. Phys. A 350 (1994) 189.
[24] H. Schnare, G. Winter, L. Käubler, J. Reif, R. Schwengner, J. Döring, G.D. Johns, S.L. Tabor, C.J. Gross, Y.A. Akovali, C. Baktash, D.W. Stracener, F.E. Durham, P.F. Hua, M. Korolija, D.R. LaFosse, D.G. Sarantites, I.Y. Lee, A.O. Macchiavelli, W. Rathbun, A. Vader Molen, Phys. Rev. C 56 (1997) 729.
[25] A.A. Chishti, W. Gelletly, C.J. Lister, B.J. Varley, Ö. Skeppstedt, J. Phys. G 16 (1990) 481.
[26] J. Heese, K.P. Lieb, S. Ulbig, B. Wörmann, J. Billowes, A.A. Chishti, W. Gelletly, C.J. Lister, B.J. Varley, Phys. Rev. C 41 (1990) 603.
[27] S. Suematsu, S. Mitarai, J. Mukai, H. Tomura, A. Odahara, T. Kuroyanagi, S.E. Arnell, O. Skeppstedt, D. Jerrestam, J. Nyberg, A. Atac, H. Roth, G. Sletten, in: Kyushu Univ. Tandem Acc. Report 1991–1992, 1993, p. 72.
[28] C.J. Gallagher, S.A. Moszkowski, Phys. Rev. 111 (1958) 1282.
[29] I. Ragnarsson, P.B. Semmes, Hyp. Int. 43 (1988) 425.
[30] F. Iachello, A. Arima, The Interacting Boson Model, Cambridge University Press, Cambridge, 1987.
[31] F. Iachello, O. Scholten, Phys. Rev. Lett. 43 (1979) 679.
[32] V. Paar, in: Zs. Dombrádi, T. Fenyes (Eds.), In-Beam Nuclear Spectroscopy, Akadémiai Kiadó, Budapest, 1984, Vol. 2, p. 675.
[33] D. Bucurescu, G. Căta, D. Cutoiu, G. Constantinescu, M. Ivaşcu, N.V. Zamfir, Nucl. Phys. A 401 (1983) 22.
[34] D. Bucurescu, G. Căta, M. Ivaşcu, N.V. Zamfir, C.F. Liang, P. Paris, J. Phys. G 14 (1988) L175.
[35] O. Scholten, Computer codes PHINT and FBEM, KVI Report No. 63, 1979.
[36] O. Scholten, Computer codes ODDA and PBEM, KVI Report No. 252, 1982.
[37] O. Scholten, IBFFM code, 1988, unpublished.
[38] W.-T. Chou, W.C. McHarris, O. Scholten, Phys. Rev. C 37 (1988) 2834.
[39] R. Bengtsson, S. Frauendorf, Nucl. Phys. A 327 (1979) 139.
[40] I. Hamamoto, Phys. Lett. B 235 (1990) 221.
[41] G.B. Hagemann, J.D. Garrett, B. Herskind, G. Sletten, P.O. Tjøm, A. Henriquez, F. Ingebretsen, J. Rekstad, G. Løvhøiden, T.F. Thorsteinsen, Phys. Rev. C 25 (1982) 3224.
[42] F. Dönau, Nucl. Phys. A 471 (1987) 469.
[43] R.B. Firestone, V.S. Shirley, Table of Isotopes, Wiley, New York, 1996, Appendix E. Nuclear Moments.
[44] E.F. Moore, P.D. Cottle, C.J. Gross, D.M. Headly, U.J. Hüttmeier, S.L. Tabor, W. Nazarewicz, Phys. Rev. C 38 (1988) 696.
[45] R.F. Davie, D. Sinclair, S. Ooi, N. Poffe, A. Smith, H.G. Price, C.J. Lister, B.J. Varley, I.F. Wright, Nucl. Phys. A 463 (1987) 683.
[46] S.E. Arnell, C. Ekström, L.P. Ekström, A. Nilsson, I. Ragnarsson, P.J. Smith, E. Wallander, J. Phys. G 9 (1983) 1217.
[47] E.F. Moore, P.D. Cottle, C.J. Gross, D.M. Headly, U.J. Hüttmeier, S.L. Tabor, W. Nazarewicz, Phys. Lett. B 211 (1988) 14.
[48] D.H. Smalley, R. Chapman, P.J. Dagnall, C. Finck, B. Haas, M.J. Leddy, J.C. Lisle, D. Prevost, H. Savajols, A.G. Smith, Nucl. Phys. A 611 (1996) 96.